

Kinetic Characteristics of Phonons and the Structural Heterogeneities of the Monoaluminate $Y_{1-x}Er_xAlO_3$ Solid Solutions

I. E. Lezova^a, O. V. Karban^b, A. V. Taranov^{c,*}, E. N. Khazanov^{c,**}, and E. V. Charnaya^a

^a St. Petersburg State University, St. Petersburg, 199034 Russia

^b Izhevsk State Agricultural Academy, Izhevsk, 426069 Russia

^c Kotel'nikov Institute of Radio Engineering and Electronics, Russian Academy of Sciences, Moscow, 125009 Russia

*e-mail: taranov@cplire.ru

**e-mail: khazanov@cplire.ru

Received June 19, 2019; revised July 24, 2019; accepted July 26, 2019

Abstract—The low-temperature specific heat, the transport characteristics of phonons at the helium temperatures, and the nanostructural heterogeneities in the erbium monoaluminate $YAlO_3:Er$ solid solution single crystals synthesized by directional solidification are studied.

DOI: 10.1134/S1063776120010070

1. INTRODUCTION

Like yttrium–aluminum $Y_3Al_5O_{12}$ (YAG) garnets, yttrium $YAlO_3$ monoaluminates are synthesized from the Y_2O_3 yttrium oxide and the Al_2O_3 aluminum oxide taken in proportions of 1 : 3 and 1 : 1, respectively. When doped by rare-earth (RE) ions, both materials meet the requirements of quantum electronics as active laser media and have a high mechanical strength, a good thermal conductivity, a high transparency, and a good combination of spectral properties [1].

YAG single crystals are cubic and optically homogeneous. Therefore, YAG:Re (Re = rare-earth metal) was used to fabricate polycrystalline ceramics, the efficiency of which is comparable with that of single crystals and some their mechanical properties exceed those of single crystals [2]. The monoaluminates have the orthorhombic lattice with parameters $a = 0.5179$ nm, $b = 0.5329$ nm, and $c = 0.77370$ nm and are biaxial. The monoaluminate-based laser rods along axis b can be used for powerful amplification at a low threshold and along the c axis, for weak amplification and energy accumulation in the Q-switch mode [3].

The neodymium-doped monoaluminates [4] have good laser characteristics, which can be comparable with those of YAG:Nd. They can assimilate a higher activator concentration as compared to YAG single crystals [5]. On the other hand, aluminates suffered from a number of uncontrollable defects, which restricted their competition with YAG. Like YAG:Re, the $YAlO_3:Re$ contains fragments of Re_3Al and Al_3Re

layers [1], and the Re–Al distance in both layers corresponds to this distance in oxides. The processes of defect formation in $YAlO_3:Re$ and YAG:Re during their synthesis from oxides are thought to be similar. The nonstoichiometry of a solid-solution composition is usually related to the possibility of substitution of yttrium and RE ions for the Al sites (in YAG, in the octahedral surrounding of oxygen) [6].

Unlike $YAlO_3$ and $YAlO_3:Nd$, $YAlO_3:Er$ single crystals are nontransparent at photon energy $\nu > 35000$ cm^{-1} [8], which is likely to be related to the defects of color center formation. The spectrum of additional absorption after γ irradiation of $YAlO_3:Er$ differs substantially from that of $YAlO_3:Nd$, which is likely to be caused by a change in the defect subsystem during the $Y^{3+} \leftrightarrow Er^{3+}$ substitution [7].

We could expect the appearance of immiscibility regions in $YAlO_3:Er$ single crystals; however, X-ray diffraction analysis did not reveal such heterogeneities. However, the NMR investigations [8] of the $YAlO_3:Er$ solid solutions synthesized by directional solidification found their tendency toward clustering with the formation of various phase microregions.

The purpose of this work is to analyze the low-temperature specific heat and the kinetic characteristics of thermal-frequency phonons in the helium-temperature range and to study the structure of the solid solutions in the $YAlO_3:Er$ aluminates synthesized by directional solidification.

2. EXPERIMENTAL

Monoaluminate $Y_{1-x}Er_xAlO_3$ ($x = 0.07, 0.1, 0.15, 0.2, 0.45$) solid-solution samples were studied by the following three techniques.

The temperature dependences of specific heat $c(T)$ were investigated on a PPMS-9 + Ever-Cool-II (Quantum Design) device in a zero magnetic field in the temperature range 1.9–220 K.

The method of analyzing the transport of nonequilibrium phonons (NPs) in the diffusion mode in single crystals was described in detail in [9]. This method is based on heating a metallic (Au) NP injector film by a short (shorter than 100 ns) current pulse to temperature T_h such that $\Delta T = T_h - T_0 \ll T_0$. The phonons are weakly nonequilibrium and the sample has the thermostat temperature. As a result, we can study the temperature dependences of NPs by changing thermostat temperature T_0 . NP pulses are recorded by a broadband superconducting bolometer (Sn) on the sample face that is opposite to the injector. The excess of the bolometer temperature over the equilibrium temperature is described by the solution to the nonstationary diffusion equation

$$\Delta T(t) \propto t^{-1/2} \exp\left(-\frac{L^2}{4D(T)t}\right), \quad (1)$$

where L is the sample length along the NP propagation. The measurements were carried out within the linear segment of the bolometer characteristic, where $S \propto \Delta T$. We measured the time of recording the maximum signal ($t_m(T)$), which is uniquely related to diffusion coefficient $D(T)$, $t_m = L^2/2D$ (“plane” geometry). Under elastic (Rayleigh) scattering conditions, according to Eq. (1) we have $D(T) = D_0(T) = (1/3)v^2\tau_0 \propto T^{-4}$ ($v = 5.4 \times 10^5$ cm/s is the polarization-averaged velocity of sound, τ_0 is the elastic scattering time), and the trailing edge of the signal to be recorded is $S(t) \propto t^{-1/2}$. When measuring the time characteristics, we were able to avoid the necessity of bolometer calibration during comparison measurements.

Taking into account the inelastic phonon–phonon processes induced by the anharmonicity of a crystal lattice can change an NP distribution and affect the result of measuring t_m . Only decay processes among the three-phonon processes can be effective at the helium temperatures [10]. In a one-dimensional case, diffusion length l_{ph} during the life of a phonon with respect to the lattice-anharmonicity-induced decay is

$$l_{ph}(\omega) = \sqrt{D_0(\omega)\tau_{ph}(\omega)}, \quad (2)$$

where $\tau_{ph}(\omega)$ is the inelastic phonon–phonon scattering time with respect to spontaneous decay. As will be shown below, the typical value $D_0 \approx 10^5$ cm²/s corresponds to the phonon lifetime with respect to elastic scattering ($\tau_0 = 10^{-7}$ – 10^{-6} s).

The theoretical estimation of $\tau_{ph}(\omega)$ [11] for thermal-frequency phonons at the helium temperatures and the experimental observation at $T = 3$ K [12] give $\tau_{ph}(\omega) = 10^{-3}$ – 10^{-2} s. This finding allowed one to exclude the influence of lattice-anharmonicity-induced inelastic scattering in samples of length $L < 1$ cm. NP scattering in this case is only determined by the structural features of the material. This method can be informative for analyzing the elastic phonon scattering induced by the difference between the ion masses at substitution sites [13] and the low-energy Schottky-like excitations induced by magnetic ion–ion interaction [9]. Taking into account the inelastic processes of trapping–reemission by two-level systems (TLSs) can retard the arrival of the signal maximum and elongate its trailing edge. The phonon range (l_R) and range time (τ_R) with respect to scattering (trapping) by TLS can be estimated from the diffusion theory equation

$$l_R = \sqrt{D_0\tau_R} \geq L, \quad (3)$$

which is similar to Eq. (2).

Nanometer-scale images of the cleavage surfaces of samples were studied at room temperature with a P4-SPM-MTD scanning probe microscope operating in the tapping mode of atomic force microscopy (AFM). Commercial silicon rectangular SC12 cantilevers were used. Using sequential double scanning of each row and detecting a relief in the first pass and a lateral force distribution in the second pass, we were able to obtain a microtopographic image and local physicochemical characteristics (in particular, friction forces) of the same region on the sample surface. The differences between the physicochemical properties of different regions manifested themselves in the form of bright and dark spots in AFM images in the friction force mode. The largest scanning area was 7×7 μm^2 .

3. RESULTS AND DISCUSSION

Figure 1 shows the temperature dependences of the specific heat of some $Y_{1-x}Er_xAlO_3$ solid solutions at low temperatures. The specific heat at the helium temperatures is seen to be determined by low-energy excitations. The energy of the lowest excited level of the $^4I_{15/2}$ multiplet of the Er^{3+} ion in $YAlO_3:Er$ is about 51 K (28 K in $YAG:Er$); that is, the energies in both cases are too high to explain the detected features.

Similar dependences were observed earlier in some single crystals of Er-containing solid solutions, namely, $YAG:Er$ [14], $TmAG:Er$ [15], and $GGG:Er$ [16]. As was shown in [9], the low-energy excitations in $YAG:Er$ are caused by the Kramers nature of the Er^{3+} ion, when the degeneracy of the ground level can be removed in a “zero” applied magnetic field due to the interaction of the magnetic moments of neighboring ions. As was shown in [14], the ground level splitting energy in $YAG:Er$ in the solid solution concentra-

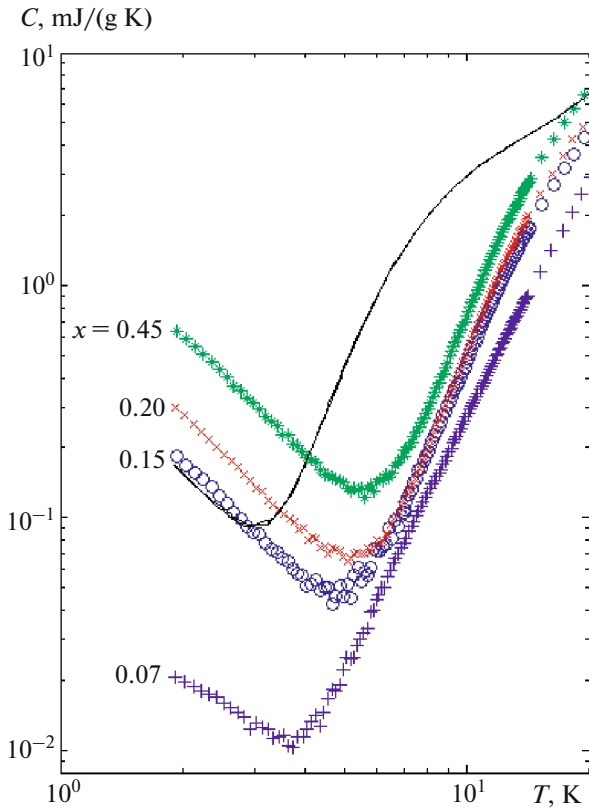


Fig. 1. (Color online) Temperature dependences of the specific heat of the $Y_{1-x}Er_xAlO_3$ solid solutions at various x (indicated at the curves) and (solid line) $Y_{2.4}Er_{0.6}Al_5O_{12}$.

tion range under study is $\Delta = 1$ K. Figure 1 shows the dependence of 20% YAG:Er ($Y_{2.4}Er_{0.6}Al_5O_{12}$). Note that the $C(T)$ dependences of the same Er contents in both materials are close at the helium temperatures, which indicates common nature of the low-energy excitations in them.

The main mechanism of elastic scattering of thermal-frequency phonons in substitutional solid solutions is scattering by the mass “defect” of the ions at substitutional sites, $Y^{3+} \leftrightarrow Re^{3+}$. The efficiency of this scattering mechanism can be accurately calculated in cubic solid solution single crystals and was comprehensively studied in YAG:Re in [13].

Figure 2 shows the concentration dependence of the elastic scattering in YAG:Re solid solutions at $T = 3.4$ K, which is normalized by the sample length squared in the direction of thermal pulse propagation (data were taken from [13]). The dashed lines at the top of Fig. 2 depict the concentration dependence with allowance for the contribution of the inelastic scattering by TLS in YAG:Er [17]. Figure 2 also shows the concentration dependences of $YAlO_3$:Re (Re = Lu, Er) single crystals. The increase in the data obtained for $YAlO_3$:Er at concentrations of 7% and 10% points to an increase in the elastic scattering rather than to

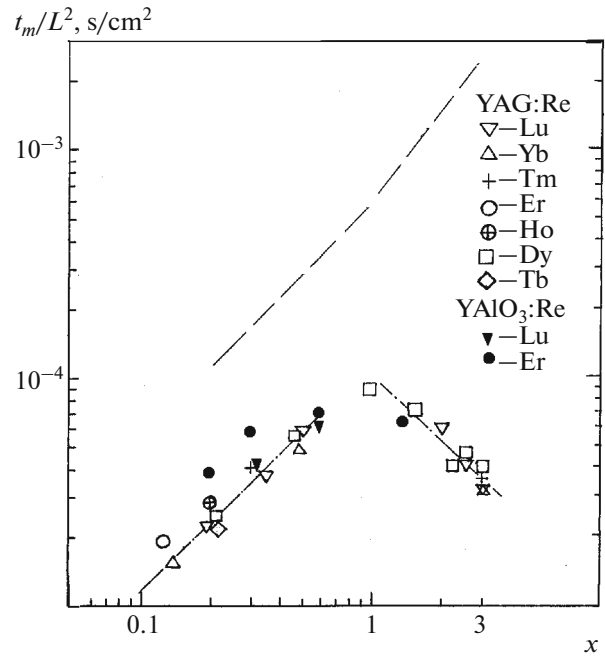


Fig. 2. Concentration dependence of the elastic scattering in the YAG:Re and $YAlO_3$:Re solid solutions at $T = 3.4$ K normalized by the sample length squared.

scattering by TLS. This finding allows us to assume that the excess of t_m/L^2 for $YAlO_3$:Er in Fig. 2 over the rate of increase of scattering by the mass defect can be related to an additional mechanism of scattering by structural defects, which are inherent in solid solutions. The data obtained for $YAlO_3$:Lu are well approximated by the t_m/L^2 calibration curve, and the phonon scattering is only determined by the difference between the masses at substitutional sites $Y \leftrightarrow Re$, as in YAG:Re.

Figure 3 demonstrates the difference between the experimental dependences obtained for the 7% compositions YAG:Er and $YAlO_3$:Er. Effective trapping and reemission during the phonon–TLS interaction in YAG:Er retard and broaden the signal maximum in YAG, and only elastic scattering is present in the $YAlO_3$:Er sample. The scattering by TLS in $YAlO_3$:Er manifests itself only in the samples with 45% impurity.

Figure 4 shows the trailing edges of the detected signals in the $YAlO_3$:Er samples of all concentrations under study at $T = 3.8$ K in the log–log coordinates. Curves 1–4 are smoothed for clarity. The signal is elongated only in the samples with 45% impurity, which indicates effective NP scattering by TLS. For the other concentrations, the decay of the trailing edge has the form $S(t) \propto t^{-1/2}$, as would be expected for elastic phonon scattering in classical diffusion. This finding means that the phonon range with respect to trapping by TLS in these samples is $l_R > L$ and τ_R is longer

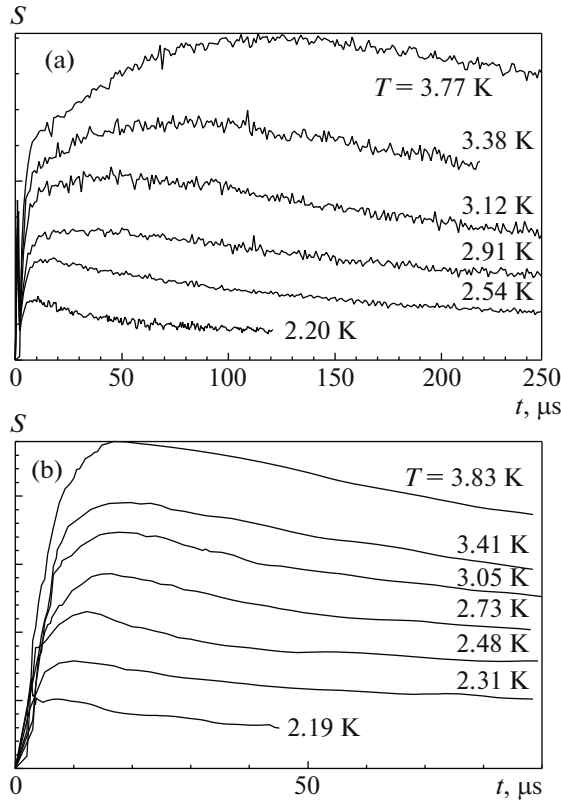


Fig. 3. NP signals at various temperatures in samples (a) YAG:Er 7%, $L = 0.68$ cm and (b) YAlO_3 :Er 7%, $L = 0.76$ cm at various temperatures.

than that in the YAG:Re samples of analogous concentrations [9] by several times. In other words, the phonon scattering by TLS in aluminates with 7% and 10% erbium at the helium temperatures cannot compete with more effective elastic scattering.

Figure 5 shows the temperature dependences of diffusion coefficient $D(T)$. When the temperature (phonon energy) increases, the dependences of a number of compositions change from Rayleigh (proportional to T^{-4}) to geometric (independent of T). The temperature dependences of this scattering can be described by the formula $D = AD_0 + B$ [18], which corresponds to nonresonance scattering by structural heterogeneities (e.g., foreign-phase inclusions). Here, the first term,

$$A = \frac{9}{2} \left(\frac{x}{1-x} \right)^2$$

(where $x = \rho_1 v_1^2 / \rho_0 v_0^2$; ρ_0 and ρ_1 are the densities of the base and additional phases, respectively; v_0 and v_1 are the polarization-averaged velocities of sound in the base and additional phases, respectively) describes the Rayleigh scattering and is determined by all defects in the system, which can be considered as point defects in the long-wavelength limit. This estimate was made

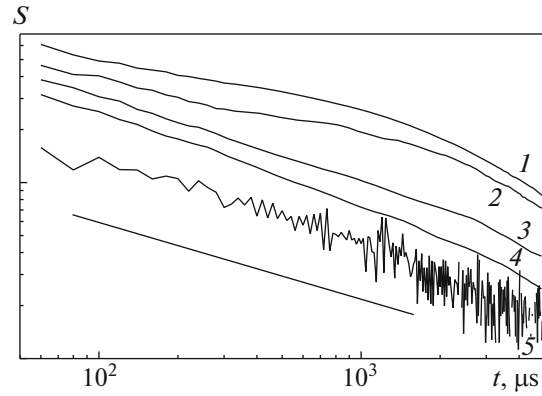


Fig. 4. Time dependences of the trailing edges of the detected signals in $\text{Y}_{1-x}\text{Er}_x\text{AlO}_3$ samples in the log-log coordinates: (1) $x = 0.45$, $T = 3.85$ K; (2) $x = 0.45$, $T = 3.4$ K; (3) $x = 0.2$, $T = 3.4$ K; (4) $x = 0.1$, $T = 3.4$ K; and (5) $x = 0.07$, $T = 3.4$ K. The straight line corresponds to the relation $S \propto t^{-1/2}$.

on the assumption of the presence of two phases, namely, YAlO_3 and $\text{Y}_{1-x}\text{Er}_x\text{AlO}_3$. The second term,

$$B = \frac{2v_0 R}{3c}$$

is determined by geometric scattering by inclusions of size $R \geq \lambda$ and volume fraction c . Estimation demonstrates that the phonon wavelength is $\lambda \sim 30\text{--}40$ nm ($c \approx 0.1$) at $T = 3$ K (where scattering by heterogeneities is “turned on”).

The solid line in Fig. 5 corresponds to the relation $D(T) \propto T^{-4}$ in the $\text{Y}_{0.8}\text{Lu}_{0.2}\text{AlO}_3$ sample synthesized by the Czochralski technique, and this relation only reflects the elastic diffusion scattering by the ion mass defect $\text{Y}^{3+} \leftrightarrow \text{Lu}^{3+}$ at substitutional sites.

Therefore, the results presented above demonstrate that, in the helium temperature range in the absence of the inelastic phonon–phonon interaction induced by lattice anharmonicity in YAlO_3 :Er solid solution single crystals, the scattering of thermal-frequency phonons is caused by elastic scattering by ion substitutional sites and nanostructural heterogeneities in a solid solution when the average heterogeneity size is comparable with phonon wavelength λ or exceeds it. The separation into RE-ion-lean and RE-ion-rich regions at a retained homogeneous structure of a solution was observed in the YAG:Er and YAG:Ho single crystals synthesized by directional solidification [19].

AFM investigation of the cleavage surfaces of the $\text{Y}_{1-x}\text{Er}_x\text{AlO}_3$ solid solution single crystals revealed nanoregions with different physicochemical characteristics. The structure consists of alternating bands of different brightness 20–100 nm wide depending on the doping element concentration. Figure 6 shows a friction force image of $\text{Y}_{0.8}\text{Er}_{0.2}\text{AlO}_3$.

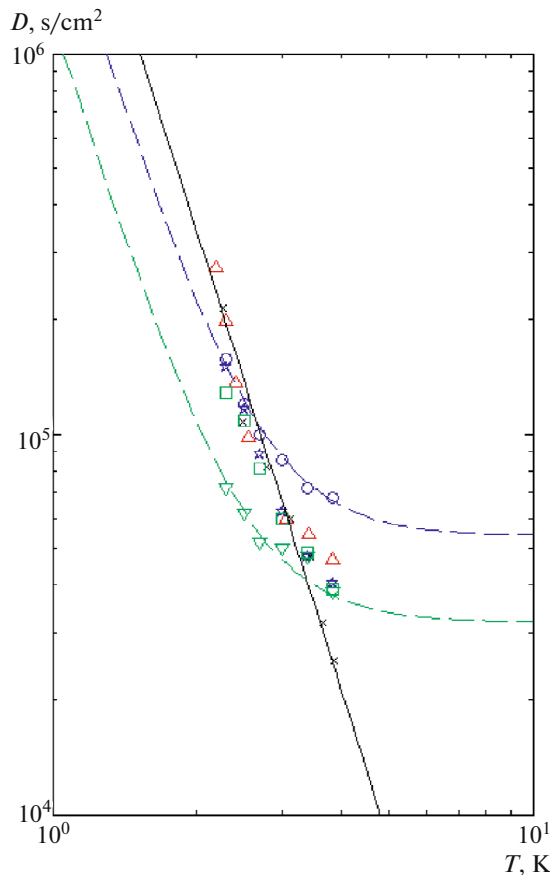


Fig. 5. (Color online) temperature dependences of diffusion coefficient $D(T)$ for some samples: (Δ) $Y_{0.8}Er_{0.2}AlO_3$, (\circ) $Y_{0.93}Er_{0.07}AlO_3$, (\star) $Y_{0.9}Er_{0.1}AlO_3$, (∇) $Y_{0.85}Er_{0.15}AlO_3$, (\square) $Y_{0.55}Er_{0.45}AlO_3$, and (\times) $Y_{0.8}Lu_{0.2}AlO_3$ synthesized by the Czochralski technique. (solid line) Relation $D \propto T^{-4}$ and (dashed lines) approximation by the formula $D = AD_0 + B$.

Since polar surface probes (silicon oxide) were used, the decrease in the capillary forces indicates a decrease in the polar surface and an increase in the

hydrophobic behavior. Obviously, the surface of the erbium-rich phase has a higher chemical activity.

The dependence of the friction forces on the scanning speed was studied in the range 0.9–45 $\mu\text{m/s}$. An increase in the scanning speed weakly affected the contrast of regions with weak changes in the chemical composition. Local regions with the same crystal structure but different RE element contents can be reliably distinguished in smooth low-roughness surfaces (root-mean-square roughness $S_q < 5$ nm).

Therefore, the specific features of the low-temperature specific heat are shown to be caused by the low-energy excitations of the Er^{3+} ion, which are related to the Kramers nature of the ion. Specifically, the degeneracy of the ground level can be removed in a zero applied magnetic field due to the interaction of the magnetic moments of neighboring ions. The ground level splitting energy in $YAlO_3:Er$ in the solid solution concentration range under study is $\Delta < 1$ K.

The longer thermal-frequency phonon range in the helium temperature range with respect to TLS trapping ($l_R > L$) in the samples under study makes it possible to estimate the kinetic characteristics of elastic scattering correctly.

The possibility of phase separation in the structure of the solid solution follows from the data on the phonon kinetics in the helium temperature range and from the AFM studies of the cleavage surfaces of the $Y_{1-x}Er_xAlO_3$ solid solution single crystals synthesized by directional solidification. Based on the dependences shown in Fig. 5, we can expect that a change in the solid solution concentration changes both the size and the concentration of the phase heterogeneities in $YAlO_3:Er$. On a macrolevel, the solid solution remains homogeneous.

FUNDING

This work was performed in terms of a state assignment in 2020 and was supported in part by the Russian Foundation for Basic Research, project no. 18-07-00191.

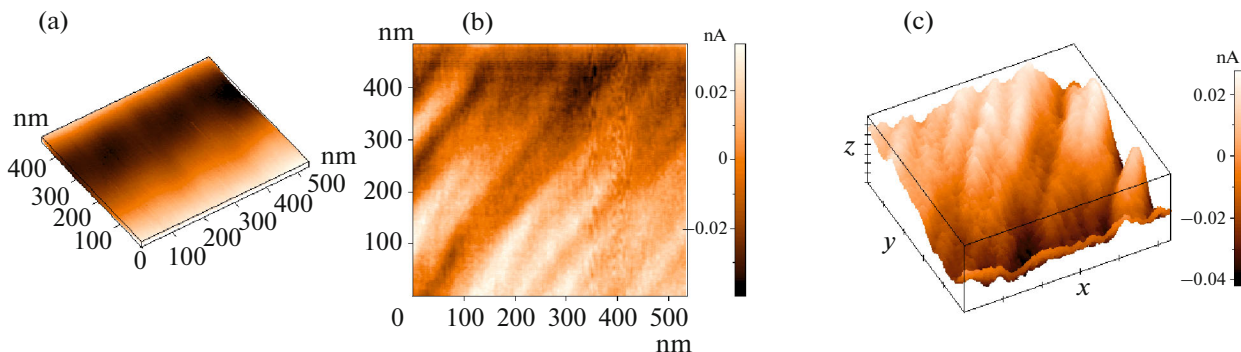


Fig. 6. (Color online) AFM images of a cleavage of the $Y_{0.8}Er_{0.2}AlO_3$ single crystal: (a) relief mode image and (b, c) friction force mode image. The scale in (c): 100 nm on axes x and y and 0.01 nA on axis z .

REFERENCES

1. R. A. Cation, *J. Solid State Chem.* **128**, 69 (1997).
2. A. A. Kaminskii, A. V. Taranov, E. N. Khazanov, and M. Sh. Akchurin, *Quantum Electron.* **42**, 880 (2012).
3. J. Kvapil, B. P. Jos Kvapil, J. Kubelka, et al., *Czech J. Phys. B* **36**, 751 (1986).
4. Kh. S. Bagdasarov and A. A. Kaminskii, *JETP Lett.* **9**, 303 (1969).
5. M. J. Weber, M. Bass, K. Andringe, et al., *Appl. Phys. Lett.* **15**, 342 (1969).
6. Jiri Kvapil, Jos Kvapil, B. Perner et al., *Cryst. Res. Technol.* **20**, 473 (1985).
7. D. Yu. Sugak, A. O. Matkovskii, Z. Frukach, A. N. Durygin, A. Suhocki, T. Lukasewicz, I. M. Sol'skii, V. Ya. Oliinyk, and A. P. Shakhov, *Inorg. Mater.* **33**, 626 (1997).
8. L. S. Vorotilova, S. N. Ivanov, V. S. Kasperovich, et al., *Sov. Phys. Solid State* **34**, 1560 (1992).
9. E. I. Salamatov, A. V. Taranov, E. N. Khazanov, E. V. Charnaya, and E. V. Shevchenko, *J. Exp. Theor. Phys.* **127**, 705 (2018).
10. I. B. Levinson, *JETP Lett.* **27**, 181 (1978).
11. I. B. Levinson, *JETP Lett.* **37**, 190 (1983).
12. S. N. Ivanov, A. V. Taranov, and E. N. Khazanov, *Sov. Phys. JETP* **72**, 731 (1991).
13. S. N. Ivanov, E. N. Khazanov, T. Paszkiewicz, et al., *Z. Phys. B* **99**, 535 (1996).
14. E. V. Shevchenko, E. V. Charnaya, E. N. Khazanov, et al., *J. Alloys Compd.* **717**, 183 (2017).
15. E. V. Charnaya, E. V. Shevchenko, E. N. Khazanov, A. V. Taranov, and A. M. Ulyashev, *J. Commun. Technol. Electron.* **64**, 811 (2019).
16. I. E. Lezova, E. V. Shevchenko, E. V. Charnaya, E. N. Khazanov, and A. V. Taranov, *Phys. Solid State* **60**, 1948 (2018).
17. E. N. Khazanov, A. V. Taranov, E. V. Shevchenko, and E. V. Charnaya, *J. Exp. Theor. Phys.* **121**, 48 (2015).
18. E. I. Salamatov, A. V. Taranov, E. N. Khazanov, E. V. Charnaya, and E. V. Shevchenko, *J. Exp. Theor. Phys.* **125**, 768 (2017).
19. O. V. Karban', S. N. Ivanov, E. I. Salamatov, and S. G. Bystrov, *Inorg. Mater.* **37**, 711 (2001).

Translated by K. Shakhlevich